

Experimental Spatial Sampling Study of the Real-Time Ultrasonic Pulse-Echo BAI-Mode Imaging Technique

Xiangtao Yin, *Student Member, IEEE*, Scott A. Morris, and William D. O'Brien, Jr., *Fellow, IEEE*

Abstract—The ultrasonic pulse-echo backscattered amplitude integral (BAI)-mode imaging technique has been developed to inspect the seal integrity of hermetically sealed, flexible food packages. With a focused 17.3-MHz transducer acquiring radio frequency (RF) echo data in a static rectilinear stop-and-go pattern, this technique was able to reliably detect channel defects as small as 38 μm in diameter and occasionally detect 6- μm -diameter channels. This contribution presents our experimental spatial sampling study of the BAI-mode imaging technique with a continuous zigzag scanning protocol that simulates a real-time production line inspection method in continuous motion. Two transducers (f/2 17.3 MHz and f/3 20.3 MHz) were used to acquire RF echo data in a zigzag raster pattern from plastic film samples bearing rectilinear point reflector arrays of varying grid spacings. The average BAI-value difference (ΔBAI) between defective and intact regions and the contrast-to-noise ratio (CNR) were used to assess image quality as a function of three spatial sampling variables: transducer spatial scanning step size, array sample grid spacing, and transducer -6-dB pulse-echo focal beam spot size. For a given grid size, the ΔBAI and CNR degraded as scanning step size in each spatial dimension increased. There is an engineering trade-off between the BAI-mode image quality and the transducer spatial sampling. The optimal spatial sampling step size has been identified to be between one and two times the -6-dB pulse-echo focal beam lateral diameter.

I. INTRODUCTION

FLEXIBLE food and pharmaceutical packages are produced by hermetically fusing opposing sheets on film seal surfaces. Sealing is the critical step in the production of flexible food and pharmaceutical packages because postprocess contamination of the processed products is frequently linked to seal and package integrity issues such as channel leaks and imperfect bonds [1]. Some microorganisms could penetrate through these defects and cause prod-

uct spoilage. The package seal integrity must be tested for potential defects formed during production because poor seal integrity could cause product loss and compromise safety, and the United States government is pressing for zero tolerance of pathogens in foods [2].

Commonly, the food processing industry uses destructive testing and visual inspection to check package seal integrity [3], [4]. Destructive testing, such as burst testing and pressure differentiation testing, only provides statistical assurance, having no safety guarantee of untested packages [4]. Visual inspection suffers from unpredictable variation and human observation limit, e.g., the smallest possible channels detectable by human observers are about 50 μm in diameter in transparent food packages. However, independent studies [4] have shown that certain microorganisms can transit through 10- μm -diameter or smaller channels. Both destructive testing and visual inspection are time consuming and expensive due to personnel costs, product loss, and unsatisfactory defect detection rates. Effective and reliable nondestructive seal integrity tests are critically needed to ensure the safety and shelf life of the food in hermetically sealed, flexible food packages.

Ultrasound evaluation techniques have many popular applications in nondestructive inspection for defects and damages embedded inside materials. The Packaging Laboratory and the Bioacoustics Research Laboratory at the University of Illinois at Urbana-Champaign, have collaborated on the development of nondestructive ultrasound pulse-echo detection methodology for food package inspection. Several ultrasound pulse-echo detection and imaging methods for food package seal integrity inspection have been developed, such as RF sample image, RF correlation-entire range image, RF correlation-specific range image, parametric ARX-modeling image, and backscattered amplitude integral (BAI)-mode image [5]–[10]. All of these methods are capable of detecting channel defects embedded in bonded two-sheet plastic package samples. However, of these methods, the BAI-mode imaging technique uses the simplest concept, has minimal implementation cost, and the image formation process is quite simple and does not require heavy computational burden [7]–[9]. The single quantity used to construct the composite BAI-mode image is called the BAI-value, and it is computed by integrating the RF echo signal envelope at each transducer sampling position. If a defect is present, the BAI-value will be different from that of the intact region because of a change in the backscattered signal. The BAI-mode imag-

Manuscript received March 8, 2002; accepted October 31, 2002. This work was supported by the Illinois Council on Food and Agricultural Research (C-FAR) Competitive Grants Program.

X. Yin was with the Bioacoustics Research Laboratory, Department of Electrical and Computer Engineering, University of Illinois at Urbana-Champaign, Urbana, IL 61801. He is now with the Dept. of Radiology, Brigham & Women's Hospital, Cambridge, MA 02139.

S. A. Morris is with the Packaging Program, Department of Food Science and Human Nutrition, University of Illinois at Urbana-Champaign, Urbana, IL 61801.

W. D. O'Brien, Jr., is with the Bioacoustics Research Laboratory, Department of Electrical and Computer Engineering, University of Illinois at Urbana-Champaign, Urbana, IL 61801 (e-mail: wdo@uiuc.edu).

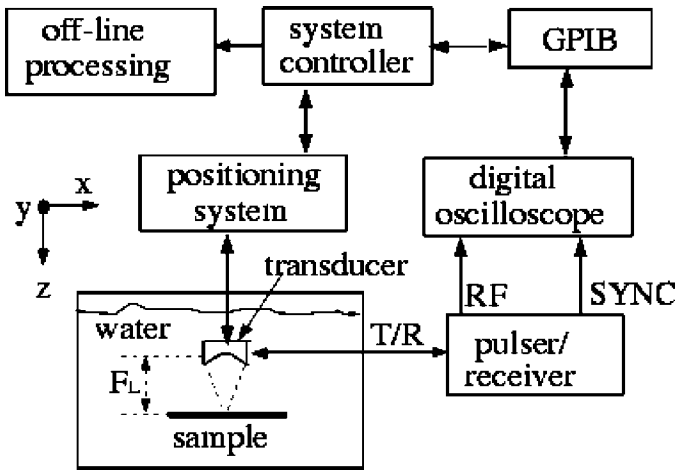


Fig. 1. Block diagram of the scanning and data acquisition system.

ing technique has demonstrated 100% detection of channels as small as $38 \mu\text{m}$ in diameter with a 17.3-MHz focused ($f/2$) transducer for the tested samples (cylindrical channels embedded in bonded two-sheet plastic package samples, thickness $110 \mu\text{m}$ per sheet). Moreover, channel defects as small as $6 \mu\text{m}$ in diameter could be intermittently detected.

In our previous studies [7]–[10], pulse-echo RF data were acquired by an ultrasonic transducer in a static rectilinear stop-and-go scanning pattern. The sample had to remain motionless until the transducer finished acquiring RF echo waveforms in the current scanning line. This static transducer scanning pattern is impractical for real-time production line package inspection because package production line motion is continuous. To simulate a real-world package production line, reported herein, a real-time zigzag raster scanning pattern whereby an ultrasonic transducer scans a moving sample simulating packaging material from above in a zigzag raster pattern.

It has been well-known that, for a pulse-echo image system, the image lateral resolution depends on the half-power beam width at focal plane [11], [12]. The Sparrow criterion for incoherent image states that the distance required to distinguish two points is defined as $d_{\text{ir}}(\text{Sparrow}) = 1.02\lambda F$, where λ is the wavelength and F is the numerical aperture of the probe [13]. However, the image quality dependency between the probe spatial sampling step size and the probe beam width has not been studied in-depth, especially in the situation in which both the target and the probe are in motion. In such a scenario, the spatial sampling pattern of the probe could affect image quality. However, it is not known if this effect is positive or negative. Thus, the real-time zigzag raster scanning pattern requires a quantitative evaluation of spatial sampling to form the BAI-mode image. The feasibility of using the two-dimensional (2-D) real-time zigzag scanning pattern to detect channel defects was demonstrated [3]. The purpose of this study is to understand how the real-time zigzag raster pattern variables affect the ultrasonic pulse-echo BAI-mode image quality and thereby advance

TABLE I
CHARACTERISTICS OF THE TDR-A AND TDR-B.

Label	TDR-A	TDR-B
Model: PANAMETRICS	V317	V317
Transducer diameter (mm)	6.35	6.35
f/number	2	3
Center frequency f_0 (MHz)	17.3	20.3
Bandwidth (MHz)	7.35	7.09
Fractional BW	43.5%	34.8%
Focal length (mm)	12.4	17.1
Pulse-echo round trip time (μs)	16.8	23.0
–6-dB beam axial depth (mm)	2.15	5.16
–6-dB beam lateral diameter (μm)	173	247

the BAI-mode imaging technique closer to being useful in real-world applications. In this study, two focused transducers were used to acquire RF data in a 2-D zigzag raster scanning pattern from plastic film samples. The samples had point reflectors arranged in a rectilinear grid of varying center-to-center distances. The BAI-mode images were constructed with the experimental data collected by each transducer for each sample. Quantitatively, the contrast-to-noise ratio (CNR) and the average BAI-value difference (ΔBAI) between defective and intact regions were assessed to evaluate the image quality versus the changing grid sizes (distance between adjacent point reflectors), the changing transducer spatial scanning step sizes, and the different ultrasonic focal beam spot sizes.

II. EXPERIMENTAL SYSTEM AND DATA PROCESSING

A. Data Acquisition System

The scanning and data acquisition system (Fig. 1) consists of focused transducer (model V317, Panametrics, Waltham, MA), four-axis (three linear and one rotational axes) precision positioning system (Daedal Inc., Harrison City, PA), pulser/receiver (model 5800PR, Panametrics), digital oscilloscope (model 9354TM, LeCroy, Chestnut Ridge, NY), system controller (Pentium[®] 166 MHz computer) and control software developed in the Bioacoustics Research Laboratory using Microsoft Visual C++ version 6.0 (Microsoft Corp., Redmond, WA).

Two immersion-type spherically focused transducers, labeled as TDR-A and TDR-B, were used. Both transducers were characterized using the pulse-echo field measurement technique (Table I) [14]. TDR-A is an $f/2$ transducer with center frequency of 17.3 MHz. TDR-B is an $f/3$ transducer with center frequency of 20.3 MHz. They have –6-dB pulse-echo focal beam lateral diameters of: $173 \mu\text{m}$ (TDR-A) and $247 \mu\text{m}$ (TDR-B). The purpose of using the two transducers was to introduce two different –6-dB pulse-echo focal beam spot sizes, yet keep the center frequency approximately the same so the effect of the beam spot size on the BAI-mode image quality could be studied.

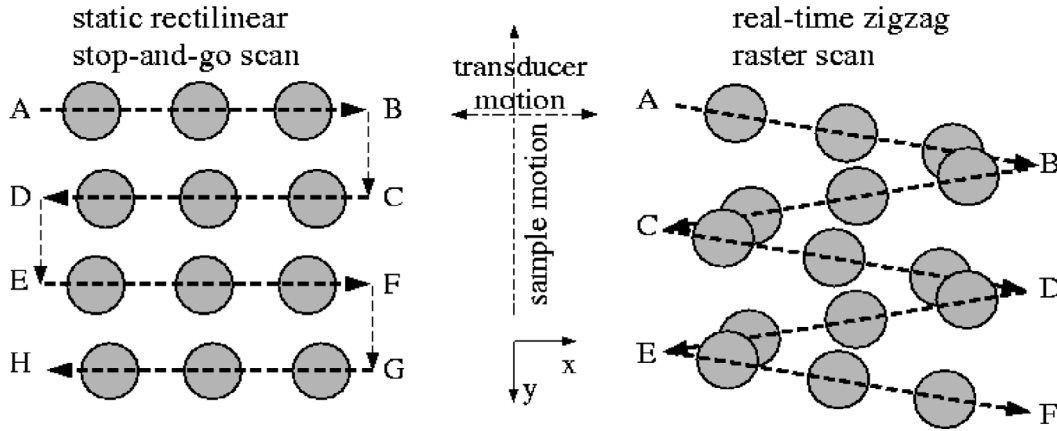


Fig. 2. Static rectilinear stop-and-go scanning pattern (left) and real-time zigzag raster scanning pattern (right). The dashed arrow lines are the transducer spatial scanning motion trajectories. The shaded circles represent the -6 -dB pulse-echo focal beam spots.

The transducer is mounted on the positioning system and immersed, together with a plastic package sample, in degassed water ($\approx 20^\circ\text{C}$). The plastic package sample is affixed to a plastic holder and placed in the focal plane of the transducer (x - y plane). The plastic package sample surface is approximately normal to the transducer beam axis (z axis). Controlled by the precision positioning system, the sample moves in the y direction and the transducer moves in the x direction. Operating in the pulse-echo mode, the transducer sends out a pulse and receives the echo signal at each scanning location (x_i, y_i) from the sample. The digital oscilloscope collects the RF echo waveform between time t_1 and t_2 at 500 Msample/sec with 256 time sequence samples at each scanning location. The 3-D ultrasound data set $\{p(x_i, y_i, t_j)$: scanning location $(x_i, y_i) \in$ planar sample surface to be scanned, sampling time instance $t_j \in [t_1, t_2]$, $j = 0, 1, \dots, 255\}$ are stored as binary data files for off-line data processing on a UNIX workstation using MATLAB[®] (The Math Works, Inc., Natick, MA).

B. Transducer Spatial Sampling Pattern

The transducer spatial sampling pattern refers to its scanning pattern during the RF data acquisition over the sample. Fig. 2 illustrates both the static rectilinear stop-and-go scanning pattern and the real-time zigzag raster scanning pattern. During RF data acquisition, the package sample moves continuously in the y direction and the transducer moves back and forth in the x direction (Fig. 2, right). The combination of sample and transducer motions yields the zigzag raster pattern. In the static stop-and-go scanning pattern, however, the sample remains motionless in the y direction but the transducer scans above the sample in the x direction.

C. Off-line Data Processing and BAI-mode Image Formation

In the off-line data processing using MATLAB[®], each RF echo signal is first Hilbert transformed to obtain its signal envelope. The BAI-value at each location then is com-

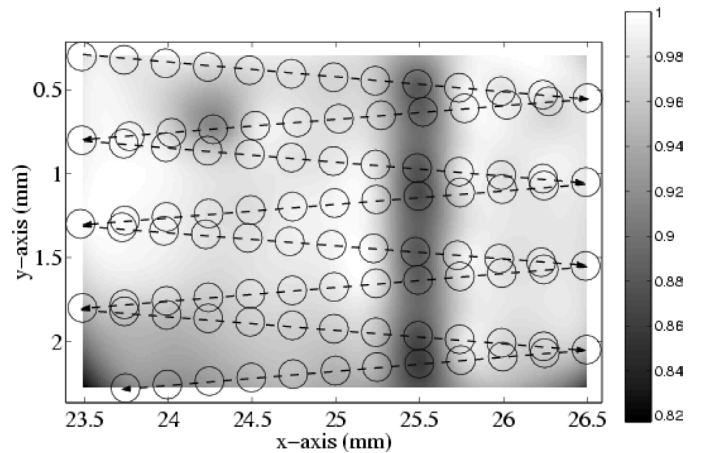


Fig. 3. A BAI-mode image showing a 2-D zigzag raster scanning pattern using TDR-A transducer. The vertical black region at $x \approx 25.5$ mm is a $38\text{-}\mu\text{m}$ -diameter, water-filled channel embedded in sealed, two-sheet plastic sample (measured speed of sound 2380 m/s, total thickness $220\ \mu\text{m}$) [9]. The $x_{\text{step}} = 0.25$ mm (center-to-center distance between two neighboring overlaid circles in the x direction), $y_{\text{step}} = 0.5$ mm (distance between two neighboring row turning points in the y direction). The circles overlaid on the zigzag raster pattern are the -6 -dB pulse-echo focal beam spots at transducer scanning locations.

puted by integrating over the entire signal envelope. The BAI-mode image is constructed from the BAI-value matrix mapped at the rectilinear grid from the zigzag raster pattern by the MATLAB[®] function ‘`griddata(...)`’ with inverse distance data interpolation option. Fig. 3 is a BAI-mode image showing a 2-D zigzag raster scanning pattern with TDR-A.

III. SPATIAL SAMPLING

The continuous zigzag raster scanning pattern simulates a real-time, on-line package inspection scenario. The purpose of the spatial sampling resolution study is to reveal the underlying factors that could affect the ultrasonic detection and image formation.

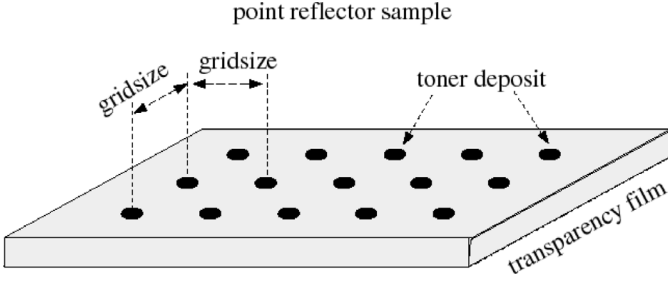


Fig. 4. A point-reflector (toner-dot) array sample on transparency film.

A. Sample Preparation

To investigate spatial sampling resolution, the BAI-mode imaging technique was applied to point-reflector samples with different rectilinear grid sizes (distance between adjacent point reflectors) and changing transducer spatial scanning step sizes. Each point reflector produces a point spread function for evaluation of the ultrasonic imaging system. Five point-reflector array samples, labeled from *a* through *e*, were made by using a 1200-DPI laser printer (Hewlett Packard LaserJet Series II-8100DN, Palo Alto, CA). The toner dots formed a rectilinear point-reflector array with different grid sizes on 114- μm -thick transparency films (CG5000 type, 3M Visual Systems Division, Austin, TX, ingredient: acrylate copolymer <94%, urea-formaldehyde polymer 1%–5%, ammonium, [3-(dodecyloxy)-2-hydroxypropyl] bis(2-hydroxyethyl)methyl-methyl sulfate (salt) <1.0%) (Fig. 4). The diameter of each toner dot was 127.2 μm . Grid spacings (center-to-center distances) were 848, 742, 636, 530, and 424 μm , respectively.

The high-resolution rectilinearly deposited toner-dot array provides a “template” of targets with nearly uniform target size and precise locations, ideal for image evaluations. Because the target strengths are uniform and the positions are well-known, the contribution to the BAI-mode image from the individual target characteristics will be suppressed to minimal. Such individual target characteristics would cause variations in target echo waveforms, which are interference factors in image evaluation and comparison. Furthermore, the round-shaped dots yield equal echo strengths in evaluating spatial sampling resolution in both the *x* and the *y* directions, rather than using defect channels with variable target strengths.

B. Spatial Sampling Variation

Three spatial sampling variables were studied by using the two transducers to perform multiple scans over the five grid sizes of toner-dot array samples with the 2-D zigzag raster scanning pattern. The transducer scanning step size and the toner-dot array grid size were varied, and the third spatial sampling variable was the -6-dB pulse-echo focal beam lateral diameter.

The scanning area was a rectangle, 3 mm in the *x* direction and 2 mm in the *y* direction. The spatial scanning

steps were variable in both *x* and *y* directions, denoted as x_{step} and y_{step} (Fig. 5). The x_{step} was defined as the center-to-center distance between two adjacent data acquisition locations in the *x* direction. The y_{step} was defined as the travel distance in the *y* direction when the transducer completed one back-and-forth scan cycle in the *x* direction.

The measured x_{step} for the data set collected from toner-dot array samples was 25 μm for all scans. Changing the x_{step} was simulated off-line by parsing step sizes at the desired sampling locations from the 3-D ultrasound data set as described in Section II. For instance, to simulate a 50- μm x_{step} and a 100- μm x_{step} from the measured x_{step} of 25- μm , RF echo waveforms were parsed every two and every four sampling locations, respectively. The x_{step} was chosen to be 25, 50, 75, 100, 125, 150, 200, 250, 300, 375, 500, 600, 750, and 1000 μm , which correspond with 121, 61, 41, 31, 25, 21, 16, 13, 11, 9, 7, 6, 5, and 4 sampling points evenly spanned in the 3-mm distance in the *x* direction, respectively. Fig. 5(a)–(c) illustrates the oversampling, critical-sampling and undersampling situations in the *x* direction compared to the -6-dB pulse-echo focal beam lateral diameter. For each sample, y_{step} was set to be 200, 300, 400, and 500 μm . Note that the y_{step} is determined by the sample’s continuous motion speed. The faster the sample moves, the larger the y_{step} is. Fig. 5(d)–(f) demonstrates the effect of sample motion speed on the y_{step} . Thus, only four scans ($x_{\text{step}} = 25 \mu\text{m}$, $y_{\text{step}} = 200, 300, 400, \text{ and } 500 \mu\text{m}$) were needed for each sample per transducer to cover 56 pairs of ($x_{\text{step}}, y_{\text{step}}$), which reduced data acquisition labor drastically.

The transducer’s scanning motion velocity \mathbf{v} has *x* and *y* components, v_x and v_y , which obeys:

$$\frac{v_y}{v_x} = \frac{y_{\text{step}}/2}{x_{\text{step}} \times (NS_x - 1)} = \frac{y_{\text{step}}}{2x_{\text{total}}}, \quad (1)$$

$$|\mathbf{v}| = \sqrt{v_x^2 + v_y^2},$$

for any given x_{step} and y_{step} , where NS_x is the total number of sampling points in the *x* direction and x_{total} is the total transducer traveling distance in the *x* direction. In the experiments, the speed $|\mathbf{v}|$ was set to be 1 mm/s for all scans to allow ample time for the experiment system to acquire RF echo data. But in practice, the speed $|\mathbf{v}|$ could be much higher as long as the following two conditions are satisfied: the time interval between two echo receptions at neighboring spatial sampling locations is greater than the pulse-echo round trip time plus the echo pulse duration, and the data acquisition hardware speed is fast enough.

C. Image Quality Evaluation

Two statistical descriptors, ΔBAI and CNR, are defined to quantitatively assess the BAI-mode image quality [9], [15].

$$\mu_b = \frac{1}{N_b} \sum_{i=1}^{N_b} \quad (2)$$

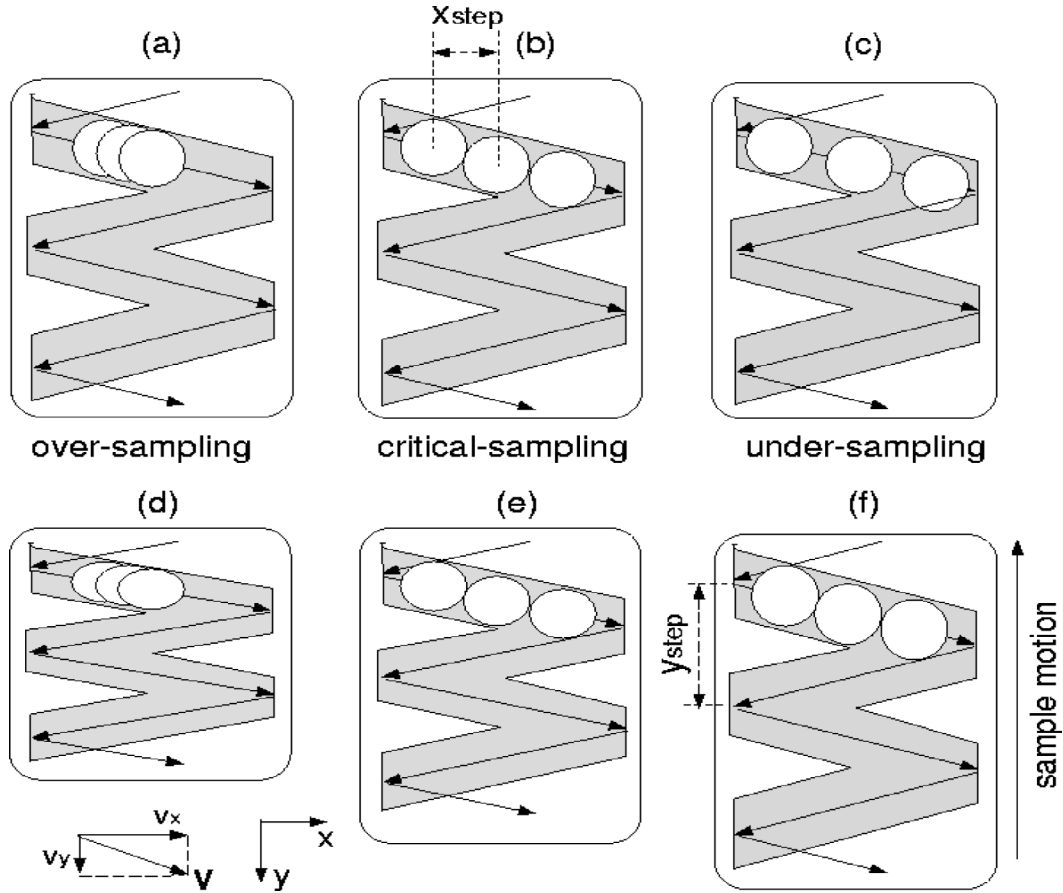


Fig. 5. Changing x_{step} [(a), (b), (c)] and changing y_{step} [(d), (e), (f)].

$$p_{b_i}, \mu_d = \frac{1}{N_d} \sum_{i=1}^{N_d} p_{d_i}, \quad (3)$$

$$\sigma_b = \left[\frac{1}{N_b} \sum_{i=1}^{N_b} (p_{b_i} - \mu_b)^2 \right]^{\frac{1}{2}}, \quad (4)$$

$$\Delta BAI = \frac{\mu_b - \mu_d}{\max_i \{p_i\}}, \quad (5)$$

$$CNR = \frac{1}{\sigma_b} \cdot \frac{\mu_b - \mu_d}{\max_i \{p_i\} - \min_i \{p_i\}}. \quad (6)$$

Subscripts b and d represent background (intact) and defective (toner dot) regions, respectively, and N_b and N_d are the total numbers of pixels in the background and the defective regions, respectively. Image pixel value p represents the corresponding BAI-value at the specific point. μ_b and μ_d are mean BAI-values for background and defective regions, respectively, and σ_b is the standard deviation of the BAI-values for the background region.

The ΔBAI (4) is defined as the difference between the average BAI-values of the background and the defective (toner dot) regions, normalized by the maximum BAI-value in the image. It represents the sensitivity of the detection method to the RF echo signal variation between background and defective regions. In terms of the signal detection theory, the CNR can be viewed as a likelihood threshold of a binary hypothesis testing in which the signal

(BAI-values in defective region) and the noise (BAI-values in background region) are both modeled as Gaussian random variables. The CNR (5) is the ratio of the average value difference between signal pixels and noise pixels to the overall dynamic range of the image pixels, divided by the standard deviation of the noise pixel values. In this sense, CNR is a measure of the robustness of the defect detection against noise. The higher the CNR is, the more distinguishable the defect image is. The pixels were selected by cropping separate rectangles in background and defective regions.

IV. RESULTS

Using the real-time zigzag raster scanning pattern, four scans were performed for each of the five samples with each transducer. Fig. 6 displays RF echo waveforms and their Hilbert transforms in two typical cases: the on-target case (solid-line waveform and dotted-line envelope) and the off-target case (dashed-line waveform and dash-dotted-line envelope). Because the point reflector (toner dot) is on the top surface of the transparency film, the major amplitude variation occurs in the front part of the RF echo waveform.

Fig. 7 shows an example of image quality as a function of x_{step} using TDR-A. The y_{step} is 200 μm . Each subimage displays the BAI-mode image for a different x_{step} . For the oversampled cases ($x_{step} \leq 200 \mu\text{m}$), there

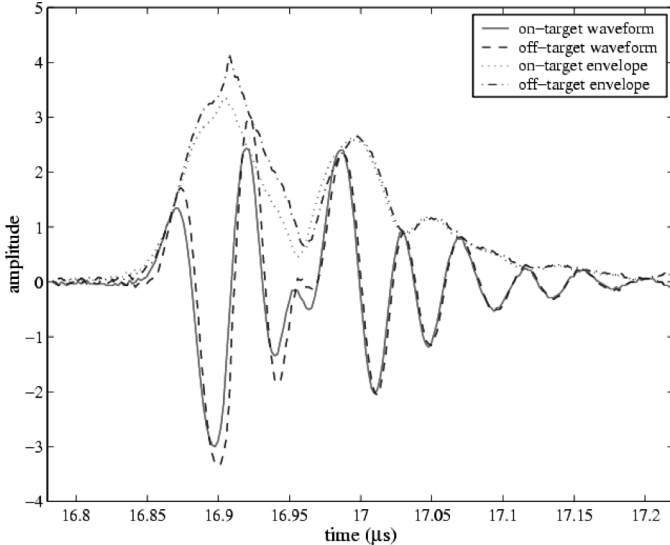


Fig. 6. The RF echo waveforms and their envelopes from point-reflector sample (single layer transparency film with a rectilinear toner-dot array), TDR-A.

was no significant change in image quality according to both subjective evaluation and quantitative assessment of the Δ BAI and CNR curves. Both curves appeared relatively flat when the x_{step} ranged in $[25 \mu\text{m}, 200 \mu\text{m}]$. For the undersampled cases ($x_{\text{step}} \geq 200 \mu\text{m}$), the image quality degraded gradually but noticeably as the x_{step} increased. Subjective assessment shows that, when the x_{step} was greater than twice the -6 -dB pulse-echo focal beam diameter ($x_{\text{step}} \geq 375 \mu\text{m}$), the BAI-mode image started losing the true details of sample structure. After x_{step} exceeded $375 \mu\text{m}$, the Δ BAI and CNR values degraded much faster than the value-dropping rate in the range of $[200 \mu\text{m}, 375 \mu\text{m}]$. But the array's point reflectors were detectable up to an x_{step} of $600 \mu\text{m}$. Even when the x_{step} was 1 mm , the transducer still was able to detect some of the point reflectors, but this was only because the ultrasound beam intercepted the toner dots.

Fig. 8 further depicts the BAI-mode images for all five samples in the oversampled, critical-sampled, undersampled, and extremely undersampled cases using TDR-A. The y_{step} is $200 \mu\text{m}$. As in Fig. 7, the image quality degraded as the x_{step} increased for all five samples.

As a comparative study of the focal beam spot diameter, the BAI-mode images using TDR-B also were obtained. Fig. 9 shows the BAI-mode image quality as a function of y_{step} using TDR-A and TDR-B. The x_{step} is $100 \mu\text{m}$. For the given x_{step} , the best image quality for TDR-A and TDR-B occurred when $y_{\text{step}} = 200 \mu\text{m}$ and $y_{\text{step}} = 300 \mu\text{m}$, respectively. After y_{step} was greater than the -6 -dB pulse-echo focal beam diameter ($173 \mu\text{m}$ for TDR-A and $247 \mu\text{m}$ for TDR-B), the BAI-mode image quality degraded as the y_{step} increased. As the spatial sampling in the y dimension became coarser, the point reflectors showed position shift and size distortion. But the three point reflectors in the middle column had less position shift and size distortion than other point-reflector columns. The spatial sampling density (the overlap extent of the -6 -dB

pulse-echo focal beam spots) of the zigzag raster pattern was higher in the central part than on the left and right margin of the image.

Fig. 10 compares the BAI-mode images using both transducers. The left three images were constructed by using TDR-A with $x_{\text{step}} = 25, 300$ and $600 \mu\text{m}$, $y_{\text{step}} = 200 \mu\text{m}$. The right three images were constructed by using TDR-B with $x_{\text{step}} = 25, 300$, and $600 \mu\text{m}$, $y_{\text{step}} = 300 \mu\text{m}$. In the oversampled case ($x_{\text{step}} = 25 \mu\text{m}$), the BAI-mode image obtained by TDR-A showed better details of each toner dot than the BAI-mode image obtained by TDR-B because of the smaller beam spot size of TDR-A. But the toner-dot array pattern was more clearly detected by TDR-B than by TDR-A when the x_{step} increased. This is because TDR-B has larger -6 -dB beam spot size so that the ratio change of the scanning step size to the -6 -dB beam spot size is less significant than TDR-A.

Fig. 11 shows the Δ BAI and CNR curves versus the spatial scanning step sizes for TDR-A. For a given point-reflector array grid size, the CNR and Δ BAI values degraded as scanning step size in each spatial dimension increased, as did the image quality. This observation was consistent with our previous spatial sampling study results for channel defects [3]. The BAI-mode image quality versus the y_{step} had been studied in [3]. This study extended the spatial sampling study in both the x and the y directions with point-like targets (refer to Section III-A), aiming to find the optimal spatial sampling step sizes in both directions by quantitative assessment. The Δ BAI curves dropped with different rates in the four different x_{step} intervals: no obvious degradation in $[25 \mu\text{m}, 200 \mu\text{m}]$, moderate degradation in $[200 \mu\text{m}, 375 \mu\text{m}]$, significant degradation in $[375 \mu\text{m}, 600 \mu\text{m}]$, and abnormal enhancement in $[600 \mu\text{m}, 1000 \mu\text{m}]$. The CNR curves had the similar behavior as the x_{step} increased, except for the last interval $[600 \mu\text{m}, 1000 \mu\text{m}]$ in which the CNR curves went asymptotically flat.

Fig. 12 shows the Δ BAI and CNR curves versus the point-reflector array grid size for TDR-A at $y_{\text{step}} = 300 \mu\text{m}$. The image quality was expected to degrade because it is more difficult to separate two toner dots as the distance between them decreases. However, the Δ BAI curves (upper plot) did not show a consistent decreasing pattern as the point-reflector array grid size reduced, i.e., the Δ BAI curve for grid sample b was above the Δ BAI curve for grid sample a , although the grid size of sample b was smaller than that of sample a . The CNR curves (lower plot) monotonically decreased as the point-reflector array grid size reduced.

Fig. 13 compares the Δ BAI and CNR curves versus the spatial scanning step sizes using both transducers at $y_{\text{step}} = 200, 500 \mu\text{m}$ for sample c . The Δ BAI and CNR values degraded as scanning step size in each spatial dimension increased. For TDR-B, the Δ BAI and CNR curves dropped with different rates in the four different x_{step} intervals: no obvious degradation in $[25 \mu\text{m}, 250 \mu\text{m}]$, moderate degradation in $[250 \mu\text{m}, 500 \mu\text{m}]$, significant degradation in $[500 \mu\text{m}, 700 \mu\text{m}]$, and asymptotically flat in

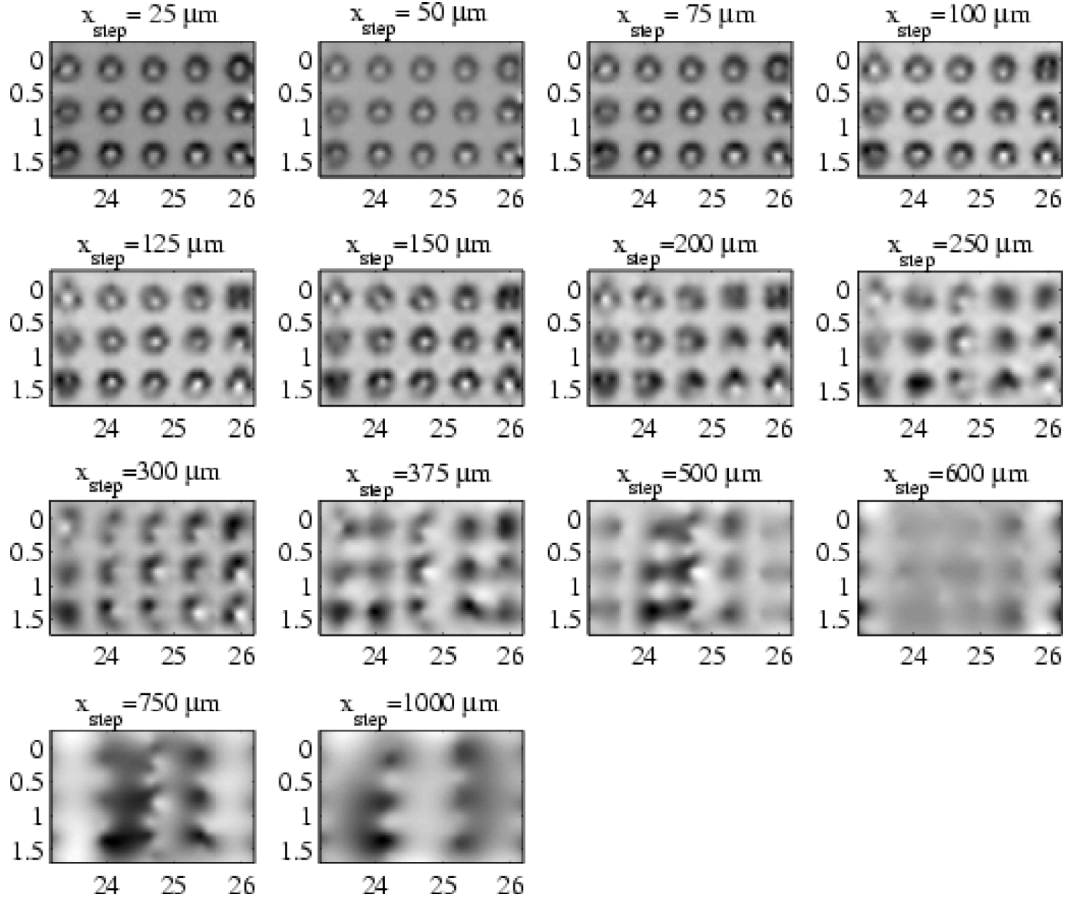


Fig. 7. Simulation of changing x_{step} using TDR-A, $y_{\text{step}} = 200 \mu\text{m}$. For each subimage, the horizontal and the vertical dimensions are the x and y axes in millimeters, respectively.

[700 μm , 1000 μm]. The rate-dropping intervals of the ΔBAI and CNR curves for TDR-A have been identified in Fig. 11 as: [25 μm , 200 μm]; [200 μm , 375 μm]; [375 μm , 600 μm]; and [600 μm , 1000 μm]. The first intervals of no obvious degradation represented the oversampled case and the upper bounds of the intervals revealed the -6-dB beam spot sizes of both transducers (200 μm for TDR-A and 250 μm for TDR-B). The second intervals of moderate degradation fell in between each of the transducer's -6-dB beam spot size and twice that size. The third and fourth intervals of significant degradation represented an extremely undersampled case. There existed a turning point between $x_{\text{step}} = 300 \mu\text{m}$ and 375 μm in the ΔBAI curves of TDR-A and a turning point between $x_{\text{step}} = 500 \mu\text{m}$ and 600 μm in the ΔBAI curves of TDR-B, after which the degradation rates of the ΔBAI values achieved their maximum. The ΔBAI curves of TDR-B changed more gradually than those of TDR-A as the x_{step} increased. The CNR value difference between $y_{\text{step}} = 200 \mu\text{m}$ and 500 μm of TDR-A was much greater than that of TDR-B.

V. DISCUSSION

In general, for those point-reflector array samples evaluated herein, the CNR and the ΔBAI values degraded

gradually as scanning step size in each spatial dimension increased for each transducer. Because the BAI-value represents the sensitivity of the detection method to the RF echo signal variation between background and defective regions, and because the CNR can be viewed as the threshold of a binary hypothesis testing, the BAI-mode image system is less sensitive to the variation of backscattered signal and less robust when the scanning step size becomes larger. Significant image quality degradation occurred after either the x_{step} or the y_{step} exceeded twice the -6-dB pulse-echo focal beam lateral diameter of each transducer. For simple detection purposes, however, the x_{step} and the y_{step} could be fairly large.

However, the BAI-mode images obtained by TDR-A (Fig. 9, upper, and Fig. 10, left) showed better defect structure details than those obtained by TDR-B (Fig. 9, bottom, and Fig. 10, right) because TDR-A has a smaller -6-dB pulse-echo focal beam spot size than TDR-B. With a larger -6-dB pulse-echo focal beam spot size, the heavily oversampled case might not be the best choice to obtain the best possible images. For example, TDR-B has a 247- μm -diameter -6-dB pulse-echo focal beam spot. The best image quality in Fig. 9, bottom, occurred when $y_{\text{step}} = 300 \mu\text{m} \geq 247 \mu\text{m}$, instead of in the oversampled case ($y_{\text{step}} = 200 \mu\text{m}$). This suggests that reducing the inspection speed of the production line below some criti-

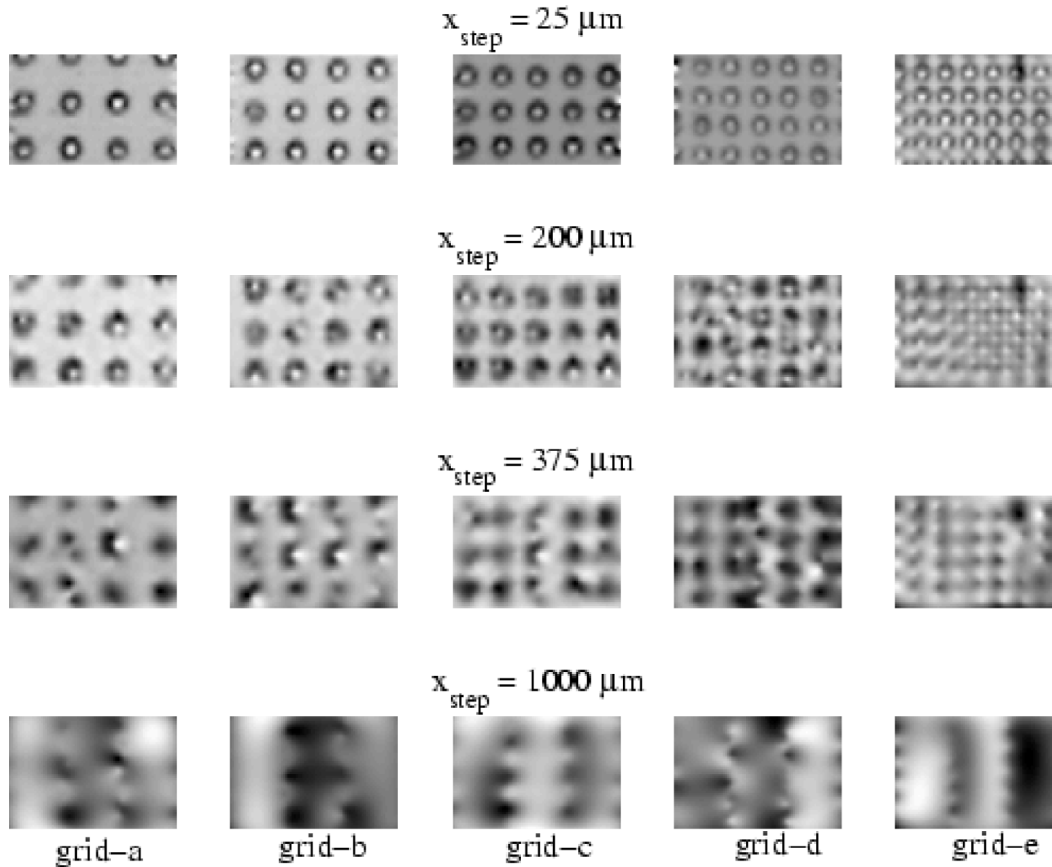


Fig. 8. Comparison of oversampled ($x_{\text{step}} = 25 \mu\text{m}$), critical-sampled ($x_{\text{step}} = 200 \mu\text{m}$), undersampled ($x_{\text{step}} = 375 \mu\text{m}$), and extremely undersampled ($x_{\text{step}} = 1000 \mu\text{m}$) situations using TDR-A. $y_{\text{step}} = 200 \mu\text{m}$. Each column represents one of the five point-reflector array samples. Each subimage takes 3 mm by 2 mm rectangle area.

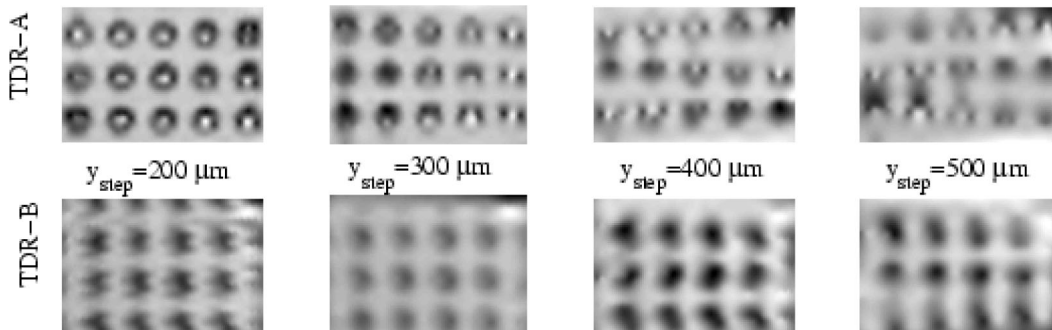


Fig. 9. Comparison of the BAI-mode images with changing y_{step} using TDR-A (upper) and TDR-B (bottom), $x_{\text{step}} = 100 \mu\text{m}$. Each subimage takes 3 mm by 2 mm rectangle area.

cal speed will not necessarily improve the defect-detection fidelity. Also in Fig. 13, the CNR values dropped as over-sampling became heavier in either the x or y direction (TDR-A and TDR-B, $y_{\text{step}} = 200 \mu\text{m}$). The heavily over-sampled case works as an aggressive smoothing filter to the images and sacrifices the image contrast. As to the undersampled situation with the same step size, TDR-B yields better detection of the array pattern than TDR-A (Fig. 10). What really matters is the ratio of the -6 -dB pulse-echo focal beam spot size to the spatial sampling step size. A small ratio offers better defect details but a

large ratio gives consistent sample pattern detection.

Image blurring was observed (Figs. 7–10) when x_{step} (scanning step size) increased, or y_{step} (scanning speed) increased. Because of the nonconstant spatial-sampled density of the zigzag raster pattern (highest density in center but lowest near margin), the BAI-mode image quality was uneven with the best quality in the center but the worst near the margin. There is a tradeoff between the BAI-mode image quality and the spatial sampling step sizes of the real-time zigzag raster scanning pattern. In other words, there is an engineering tradeoff between the BAI-

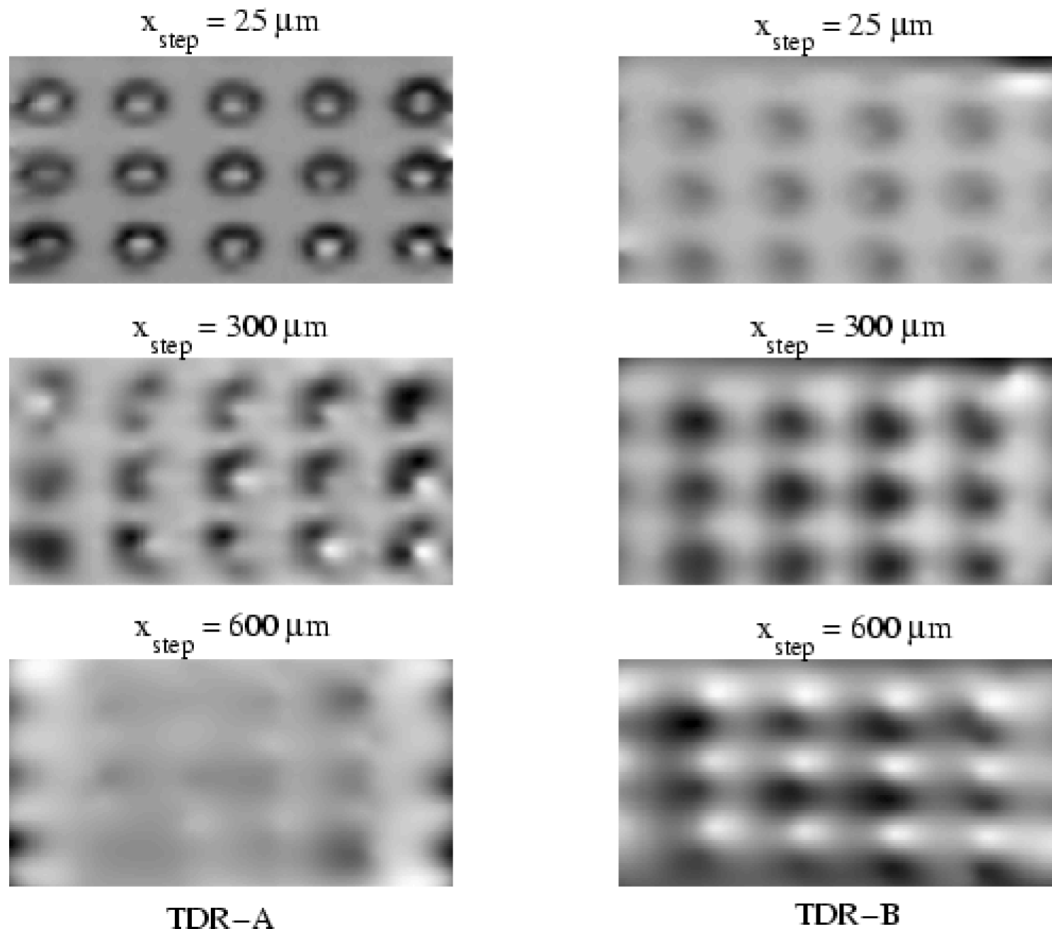


Fig. 10. Comparison of the BAI-mode images with changing x_{step} using TDR-A (left, $y_{step} = 200 \mu\text{m}$) and TDR-B (right, $y_{step} = 300 \mu\text{m}$). Each subimage takes 3 mm by 2 mm rectangle area.

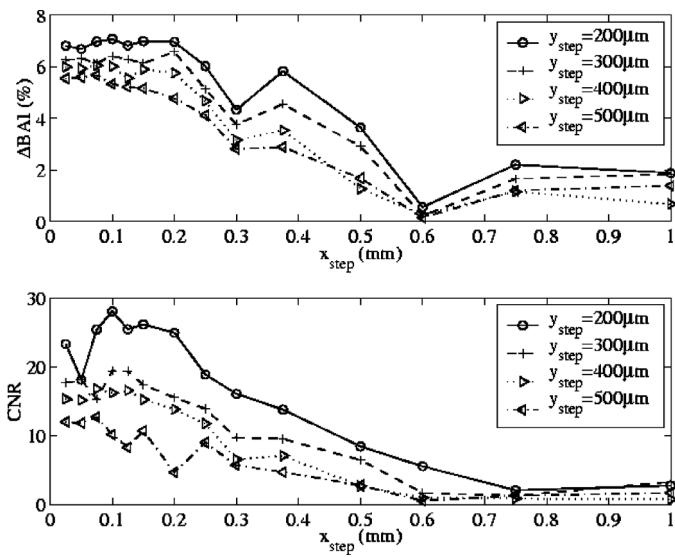


Fig. 11. The ΔBAI and CNR curves for various spatial scanning step sizes using TDR-A. The four curves in each subplot represent the four different y_{step} (200, 300, 400, and 500 μm).

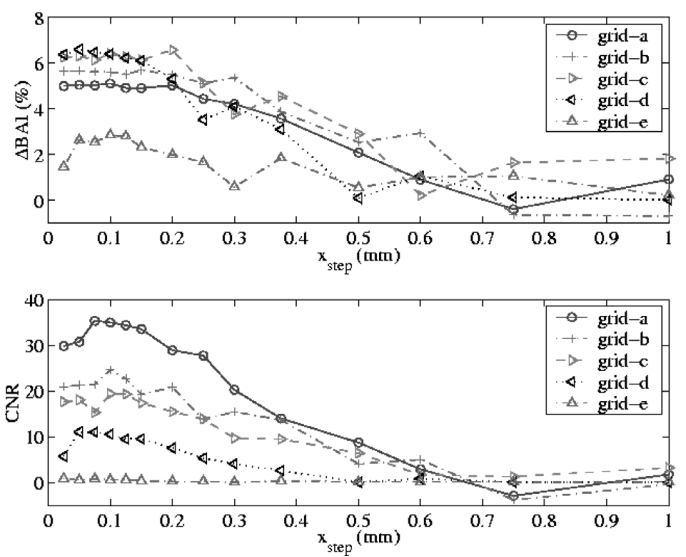


Fig. 12. The ΔBAI and CNR curves for different grid sizes using TDR-A. $y_{step} = 300 \mu\text{m}$. The five curves in each subplot represent the five samples with different grid size.

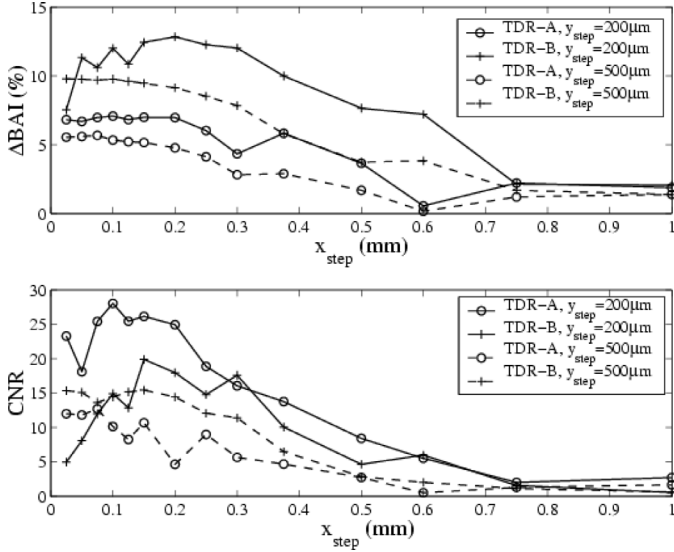


Fig. 13. The Δ BAI and CNR curves for varying spatial scanning step sizes using TDR-A and TDR-B for sample *c*. Solid lines represent $y_{\text{step}} = 200 \mu\text{m}$ cases. Dashed lines represent $y_{\text{step}} = 500 \mu\text{m}$ cases.

mode image quality and the transducer scanning speed with the zigzag raster scanning pattern.

At each sampled location and at each time instance, the focused ultrasonic transducer spatially averages over its spherical aperture the received RF echo from the sample. The envelope-integral operation (backscattered amplitude integral) sums the RF echo signal envelope temporally. The BAI-value is a quantity that describes the average characteristic of a RF echo waveform containing the sample structure information. These BAI-values then are distributed to each image pixel by inverse-distance interpolation. Although a smooth data interpolation method, the inverse-distance interpolation introduces interpolation error, especially when the given spatially sampled data points are not distributed densely enough. The more aggressive the transducer undersampling is, the coarser the sampled data points are and the more independent those BAI-values are. The structure variation of the sample could not be reconstructed with high fidelity when the spatial sampling density falls below a threshold, which is about twice that of the -6-dB pulse-echo focal beam diameter in this study ($x_{\text{step}} \geq 375 \mu\text{m}$ for TDR-A and $x_{\text{step}} \geq 500 \mu\text{m}$ for TDR-B). We hypothesize that, geometrically, a virtual -6-dB pulse-echo focal beam spot can partially or fully fit into the space between the two sampled spots because of the relative motion between transducer and sample (Fig. 14). Imagine each -6-dB pulse-echo beam spot as a half-power threshold probe, as the transducer proceeds from the left real probe to the right real probe, each real probe detects a portion of the virtual spot area, more or less. With this hypothesis, the overlapped portion between the real probes and the virtual spot works as a virtual probe that could collect information about the virtual spot area. The ideal situation is that the virtual spot area should not exceed the real spot area

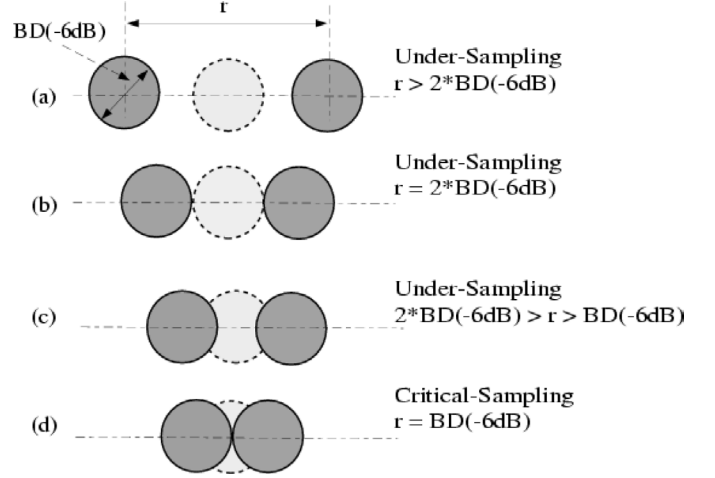


Fig. 14. Distance between -6-dB pulse-echo focal beam spots in different sampling situations. $BD(-6\text{-dB})$ is the -6-dB pulse-echo focal beam lateral diameter of the transducer. The dark circles represent actual focal beam spots. The light dashed circles are the virtual focal beam spots.

at the best because the half-power energy concentration at the transducer's focal plane is confined in the -6-dB spot size. Neither of the two real probes illuminates out of the virtual spot area when the distance is greater than twice that of the -6-dB pulse-echo beam diameter (Fig. 14). This explains why the image quality dropped significantly after the scanning step size exceeds twice the -6-dB focal beam diameter. The relative motion between the transducer and the sample effectively increased the beam spot size with the virtual probe hypothesis. Although the scanning speed is improved, increasing scanning step sizes in both spatial dimensions sacrifices the image quality. The -6-dB focal beam diameter of the focused ultrasonic transducer should be a major factor in determining the optimal transducer spatial scanning step sizes.

Based on the factors of the -6-dB pulse-echo focal beam lateral diameter and the uneven sampling density of the zigzag raster scanning pattern, we hypothesize that the optimal spatial sampling of the zigzag raster scanning pattern occurs when both the x_{step} and the y_{step} are greater than the -6-dB pulse-echo focal beam lateral diameter but less than twice of this lateral diameter. For TDR-A, the critically sampled case is $x_{\text{step}} = 200 \mu\text{m}$, $y_{\text{step}} = 200 \mu\text{m}$ in which the BAI-mode image preserves the true details of the sample structure; $x_{\text{step}} = 375 \mu\text{m}$, $y_{\text{step}} = 300 \mu\text{m}$ for rough and quick imaging; $x_{\text{step}} = 1000 \mu\text{m}$, $y_{\text{step}} = 400 \mu\text{m}$ for simple and rapid detection purpose. For TDR-B, they are $x_{\text{step}} = 250 \mu\text{m}$, $y_{\text{step}} = 300 \mu\text{m}$; $x_{\text{step}} = 450 \mu\text{m}$; $y_{\text{step}} = 400 \mu\text{m}$; and $x_{\text{step}} = 1000 \mu\text{m}$, $y_{\text{step}} = 500 \mu\text{m}$; respectively.

Suppose that the two assumptions in Section III about the scanning system were satisfied, using (1), Table II gives the estimated scanning speed using the BAI-mode imaging technique with the proposed 2-D real-time zigzag raster scanning pattern [3]. The echo pulse duration is about $0.2 \mu\text{s}$ for a $220\text{-}\mu\text{m}$ -thick package sample. The

TABLE II
ESTIMATED SCANNING SPEED FOR THE THREE TYPICAL INSPECTION CASES.

Case	TDR-A	TDR-B
$x_{\text{total}} = 5 \text{ mm}$	PRF = 56 KHz	PRF = 42 kHz
	$(x_{\text{step}}, y_{\text{step}})$ (μm), $[v_x, v_y]$ (m/s)	
Detailed imaging	(200, 200) [11.2, 0.23]	(250, 300) [10.5, 0.32]
Rough and quick imaging	(375, 300) [21.0, 0.63]	(450, 400) [18.9, 0.76]
Simple and rapid detection	(1000, 400) [56.0, 2.24]	(1000, 500) [42.0, 2.1]

pulse-echo round trip times are 16.8 μs and 23.0 μs for TDR-A and TDR-B, respectively (Table I). Consider the minimal spatial sampling time intervals required for both transducers, the pulse repetition frequency could be chosen as 56 kHz for TDR-A and 42 kHz for TDR-B, corresponding with 17.9 μs and 23.8 μs spatial sampling time intervals, respectively. The x_{total} is 5 mm, which is a typical width of plastic sealing region. For instance, if $x_{\text{step}} = 250 \mu\text{m}$ and $y_{\text{step}} = 300 \mu\text{m}$, a 5-mm distance in the x direction would require spatially sampled points (20 pulses), which would take $t_x = (\text{number of pulses})/\text{PRF} = 20/(42 \text{ kHz}) = 0.476 \text{ ms}$ for TDR-B to travel across the 5-mm distance one way. So the transducer scanning velocity x component $v_x = x_{\text{total}}/t_x = 10.5 \text{ m/s}$. Then, using (1), v_y is 0.32 m/s. They are approximately the upper speed limits for TDR-B when $x_{\text{step}} = 250 \mu\text{m}$ and $y_{\text{step}} = 300 \mu\text{m}$. The scanning speed is a function of the scanning width in the x direction; spatial sampling step sizes in both directions, which is related with focal beam width; and the pulse repetition frequency, which is limited by pulse-echo round trip time and echo-pulse duration. The inspection could be further speeded up with multiple sensors working in parallel configuration.

Because the five point-reflector array samples were scanned separately, the measurement conditions (e.g., misalignment of focusing, mechanical movement, temperature, noise) differed from each other. The ΔBAI curves for different samples were more vulnerable to the change of measurement conditions than the CNR curve. The CNR curves showed a more consistent decreasing pattern than did the ΔBAI curves when the grid size was reduced (Fig. 11). The variable measurement conditions could contribute different offset conditions to the BAI-values for each individual sample. The ΔBAI -value (4) is normalized to the maximum BAI-value in the image, which contains such offset and does not account for the overall dynamic range of pixel values. The ΔBAI -value could be a good performance index for evaluating an individual sample under different x_{step} and y_{step} , e.g., the ΔBAI curves were capable of characterizing the degradation rate change of the ΔBAI -values for each individual sample (Fig. 10), but the CNR curves failed to identify this characteristic. However, CNR (5) considers the overall dynamic range of pixel values. Furthermore, CNR is a ratio-based threshold index for evaluating image pixel values. It might suggest that CNR is a more appropriate performance index for quality assessment of the BAI-mode image, especially for the image comparison among different samples.

VI. CONCLUSIONS

The ultrasonic pulse-echo BAI-mode imaging technique with a real-time zigzag raster transducer scanning pattern was investigated experimentally. The static stop-and-go transducer scanning pattern is impractical for real-time production line package inspection because package motion is continuous. In an automated on-line package inspection system, dynamic variables such as speed and acceleration of the ultrasonic transducer relative to the continuous speed of the inspection line might contribute mechanical noise, which would adversely affect the quality of the received RF echo waveforms and consequently the ultrasonic image quality. For example, the continuous motion of the sample could cause local turbulence in the degassed water. Such a local turbulence might produce time shift and amplitude distortion when the transducer receives ultrasonic echo signals. Or even worse, the transducer might not be able to collect the entire RF echo waveform if the sample moves too fast. The zigzag raster pattern simulates the real-world package inspection scenario in which the sample is in linear motion with constant speed in the y direction while the ultrasonic transducer scans the sample back and forth in the x direction. This real-time scanning pattern offers a more efficient spatial sampling scheme on the entire sample surface and thus has the potential to examine a larger area with higher inspection speed in real-time than the stop-and-go scanning pattern could do.

By evaluating the image quality indices (ΔBAI and CNR) degradation rate, it was found that, with the proposed real-time zigzag raster transducer scanning pattern, the BAI-mode image quality depended on the relative ratio between the scanning step sizes in each spatial dimension and the -6-dB pulse-echo focal beam lateral diameter. The optimal scanning occurs when the x_{step} and the y_{step} are both greater than the -6-dB pulse-echo focal beam lateral diameter but less than twice of that. The scanning speeds related to different inspection purposes also were estimated. We conclude through the quantitative evaluation that the transducer scanning speed could be prompted with the real-time zigzag scanning pattern. The optimal spatial sampling step sizes help reduce inspection time compared to a value calculated using the Sparrow criterion [13]. For a focused ultrasonic transducer, a larger -6-dB pulse-echo focal beam spot size allows for an increased inspection speed and a better detection of the defect pattern, but does not provide for as much image detail. This is not only because the transducer's beam spot size becomes

larger but also can be attributed to the relative motion between the transducer and the sample, which effectively increases the beam width. At this stage, the preliminary investigation using rectilinear point-reflector (toner-dot) array samples [16] and this study did not include the factor of transducer center frequency. Because the center frequency will affect the image lateral resolution too, it could be another important real-time spatial sampling issue to be studied in future research.

ACKNOWLEDGMENTS

The authors would like to thank Mr. Osama Nayfeh and Mr. Jason Windedahl for their assistance with the experiments.

REFERENCES

- [1] A. Ozguler, S. A. Morris, and W. D. O'Brien, Jr., "Ultrasonic monitoring of the seal quality in flexible food packages," *Polymer Eng. Sci.*, vol. 41, no. 5, pp. 830–839, May 2001.
- [2] A. B. Blakistone, S. W. Keller, J. E. Marcy, G. H. Lacy, C. H. Hackney, and W. H. Carter, Jr., "Contamination of flexible pouches challenged by immersion biotesting," *J. Food Protection*, vol. 59, pp. 764–767, 1996.
- [3] N. N. Shah, P. K. Rooney, A. Ozguler, S. A. Morris, and W. D. O'Brien, Jr., "A real-time approach to detect seal defects in food packages using ultrasonic imaging," *J. Food Protection*, vol. 64, no. 9, pp. 1392–1398, Sep. 2001.
- [4] C. L. Harper, B. S. Blakistone, J. B. Litchfield, and S. A. Morris, "Developments in food package integrity testing," *Food Technol.*, vol. 6, no. 10, pp. 336–340, 1995.
- [5] S. A. Morris, A. Ozguler, and W. D. O'Brien, Jr., "New sensors help improve heat-seal microleak detection, part 1," *Packaging Technol. Eng.*, pp. 42–49, July 1998.
- [6] S. A. Morris, A. Ozguler, and W. D. O'Brien, Jr., "New sensors help improve heat-seal microleak detection, part 2," *Packaging Technol. Eng.*, pp. 52–68, Aug. 1998.
- [7] A. Ozguler, S. A. Morris, and W. D. O'Brien, Jr., "Evaluation of defects in seal region of food packages using the backscattered amplitude integral (BAI) technique," in *Proc. IEEE Ultrason. Symp.*, 1997, pp. 689–692.
- [8] K. Raum, A. Ozguler, S. A. Morris, and W. D. O'Brien, Jr., "Channel defect detection in food packages using integrated backscatter ultrasound imaging," *IEEE Trans. Ultrason., Ferroelect., Freq. Contr.*, vol. 45, no. 1, pp. 30–40, Jan. 1998.
- [9] C. H. Frazier, Q. Tian, A. Ozguler, S. A. Morris, and W. D. O'Brien, Jr., "High contrast ultrasound images of defects in food package seals," *IEEE Trans. Ultrason., Ferroelect., Freq. Contr.*, vol. 47, no. 3, pp. 530–539, May 2000.
- [10] Q. Tian, B. Sun, A. Ozguler, S. A. Morris, and W. D. O'Brien, Jr., "Parametric modeling in food package defect imaging," *IEEE Trans. Ultrason., Ferroelect., Freq. Contr.*, vol. 47, no. 3, pp. 635–643, May 2000.
- [11] G. S. Kino, *Acoustic Waves: Devices, Imaging, and Analog Signal Processing*. Englewood Cliffs, NJ: Prentice-Hall, 1987.
- [12] T. Sato and S. Wadaka, "Incoherent ultrasonic imaging system," *J. Acoust. Soc. Amer.*, vol. 58, no. 5, pp. 1013–1017, 1975.
- [13] A. Papoulis, *Systems and Transforms with Applications in Optics*. Melbourne, FL: Krieger Publishing, 1981.
- [14] K. Raum and W. D. O'Brien, Jr., "Pulse-echo field distribution measurement technique for high-frequency ultrasound sources," *IEEE Trans. Ultrason., Ferroelect., Freq. Contr.*, vol. 44, no. 4, pp. 810–815, July 1997.
- [15] A. Ozguler, S. A. Morris, and W. D. O'Brien, Jr., "Evaluation of defects in the seal region of food packages using the ultrasonic contrast descriptor, Δ BAI," *Packaging Technol. Sci.*, vol. 12, pp. 161–171, 1999.
- [16] X. Yin, S. A. Morris, and W. D. O'Brien, Jr., "Investigation of spatial sampling resolution of the real-time ultrasound pulse-echo BAI-mode imaging technique," in *Proc. IEEE Int. Ultrason. Symp.*, 2001, pp. 729–732.



Xiangtao Yin received his BSEE and MSEE with acoustics major from Nanjing University, China in 1994 and 1997, respectively. He entered the Ph.D. program of the Department of Electrical and Computer Engineering of University of Illinois in 1998 where he is a Ph.D. candidate.

At Nanjing University, he conducted research in simulation and design of surface acoustic wave signal processing devices for high frequency wireless communication and radar applications. At the University of Illinois, he worked as a graduate research assistant in the Center for Computational Electromagnetics to develop multilevel fast multipole hybrid FEM/BEM algorithm for large-scale scatterer RCS prediction problems from 1998 to 2000.

His current research activities involve ultrasonic nondestructive evaluation and imaging techniques, with concentration on both experimental image spatial sampling analysis and numerical modeling and evaluation of ultrasonic pulse-echo subwavelength defect detection mechanisms.



Scott A. Morris received the B.S., M.S. and Ph.D. degrees in 1981, 1987 and 1992 from Michigan State University.

While employed at Michigan State University he worked with a variety of problems related to the packaging industry: Development of an experimental permeation modeling technique utilizing a combination of numerical modeling, optical measurement techniques, and laboratory analytical testing methods. Microwave cooking of frozen and shelf-stable foods, and the redesign of their related package systems.

Improved shipping designs for retortable-pouch packaging systems. Development of chromatographic methods for the evaluation of volatile extractables from packaging materials. Determination of oxygen-barrier requirements of products that had been previously packaged in impermeable cans, and the evaluation of the suitability of producer-supplied polymeric replacements. Development of a research program in conjunction with a major packaging corporation, to test the ability of their 2-liter aseptic package to survive shipping and distribution. A survey of the state of the art of packaging in the United States, and significant trends in the technical and economic aspects of the packaging industry commissioned by the Congressional Office of Technical Assessment (OTA). Investigating the relationship of package design to the effects of shock, vibration, and compression on fresh and controlled-atmosphere-stored produce's gaseous metabolic by-products.

Since 1992 he has been at the University of Illinois where he is an Associate Professor in the departments of Food Science & Human Nutrition and Agricultural Engineering. He is currently developing a packaging research and teaching program. Current research projects within the program include: Leak detection in shelf-stable food packages' using high-frequency ultrasound, predictive modeling of package-structure permeation properties; static and dynamic structural modeling for design strength, and material-use optimization; packaging line efficiency optimization; product quality degradation from mechanical input and thermal variation; time-dependent material properties from stress-strain histories using recursive finite element algorithms; and microwave energy dispersion in food packages.

Dr. Morris is a member of the executive committee of the Institute of Food Technologists (IFT) Food Packaging Division, a member of American Society of Agricultural Engineers (ASAE), Society of Professional Engineers (SPE), Institute of Packaging Professionals (IoPP), American Society for Engineering Education (ASEE), Pi Kappa Gamma, and Gamma Sigma Delta.



William D. O'Brien, Jr. (S'64–M'70–SM'79–F'89) received the B.S., M.S., and Ph.D. degrees in 1966, 1968, and 1970, from the University of Illinois, Urbana-Champaign.

From 1971 to 1975 he worked with the Bureau of Radiological Health (currently the Center for Devices and Radiological Health) of the U.S. Food and Drug Administration. Since 1975, he has been at the University of Illinois, where he is Professor of Electrical and Computer Engineering and of Bioengineering, College of Engineering; Professor of Bioengi-

neering, College of Medicine; Professor of Nutritional Sciences, College of Agricultural, Consumer and Environmental Sciences; a Research Professor in the Beckman Institute for Advanced Science and Technology; and a Research Professor in the Coordinated Science Laboratory. He is the Director of the Bioacoustics Research Laboratory. His research interests involve the many areas of ultrasound-tissue interaction, including spectroscopy, risk assessment, biological effects, tissue characterization, dosimetry, blood-flow measurements, acoustic microscopy and imaging for which he has published 258 papers.

Dr. O'Brien is a Fellow of the Institute of Electrical and Electronics Engineers, the Acoustical Society of America and the American

Institute of Ultrasound in Medicine, and is a Founding Fellow of the American Institute of Medical and Biological Engineering. He was recipient of the IEEE Centennial Medal (1984), the AIUM Presidential Recognition Awards (1985 and 1992), the AIUM/WFUMB Pioneer Award (1988), the IEEE Outstanding Student Branch Counselor Award for Region 4 (1989), the AIUM Joseph H. Holmes Basic Science Pioneer Award (1993), and the IEEE Ultrasonics, Ferroelectrics, and Frequency Control Society Distinguished Lecturer (1997–1998). He received the IEEE Ultrasonics, Ferroelectrics, and Frequency Control Society's Achievement Award for 1998, and the IEEE Millennium Medal in 2000. He has served as Co-Chair of the 1981 and 2001 IEEE Ultrasonic Symposia, and General Chair of the 1988 IEEE Ultrasonics Symposium. He is Co-Chair of the 2003 IEEE Ultrasonics Symposium. He has been Secretary-Treasurer (1972–1980), Vice President (1981), and President (1982–1983) of the IEEE Sonics and Ultrasonics Group (currently the IEEE Ultrasonics, Ferroelectrics, and Frequency Control Society), and Editor-in-Chief of the *IEEE Transactions on Ultrasonics, Ferroelectrics, and Frequency Control* (1984–2001). He has been Treasurer (1982–1985), President-Elect (1986–1988) and President (1988–1991) of the American Institute of Ultrasound in Medicine. He has served on the Board of Directors (1988–1993) of the American Registry of Diagnostic Medical Sonographers, and has been Treasurer (1991–1994) of the World Federation for Ultrasound in Medicine and Biology.